RSC Advances

PAPER

View Article Online
View Journal | View Issue



Cite this: *RSC Adv.*, 2017, **7**, 6664

# A three dimensional N-doped graphene/CNTs/AC hybrid material for high-performance supercapacitors†

Zi-Ang Liu, Yuxi Tao, Xue-Zhi Song, Ming Bao and Zhenquan Tan*

How to improve the specific capacitance of electrode materials is of great research interest because it is a key factor for electrochemical capacitors. Herein we report a N-doped graphene/CNTs/AC (NGCA) mesoporous hybrid nanomaterial with three dimensional highly-dispersed structure synthesized by hydrothermal method. This NGCA hybrid nanomaterial has a high specific area of 952.92 $m^2$ $g^{-1}$, due to its mesoporous structure caused by inserted carbon nanotubes (CNTs) and activated carbon (AC), preventing the agglomeration of N-doped graphene (NG). The specific capacitance of this materials reaches 750 F $g^{-1}$ at 0.5 A $g^{-1}$ in KOH (1 M), which is attributed to the path of ion transport supported by the CNTs, the packing density of the electrode being elevated by the AC, and the synergistic effect among layered AC, CNTs and NG. In addition, the stable hybrid architecture makes significant contributions to the superior cycle stability with 81% capacitance retention after 2000 charge and discharge cycles at a current density of 5 A $g^{-1}$. The easy synthesis and the superior electrochemical properties endow the hybrid material with great potential in green energy storage systems in the future.

Received 28th November 2016
Accepted 3rd January 2017

DOI: 10.1039/c6ra27420j

www.rsc.org/advances



## Introduction

The energy crisis, a serious problem for human beings, is tremendously affecting human life as well as economic development. This is mainly because of the limited supply of fossil fuels and environmental damage caused by unclean energy sources, such as coal and any other fuels based on burning, which can create carbon dioxide and other greenhouse gases.[1–5] Consequently, energy efficient devices, such as neoteric energy storage, transformation devices, clean and reproducible energy sources, must emerge immediately and be constantly pursued to meet our future requirements and follow the new age lifestyle. During the past decades, more and more attention has been paid to the methods to harvest energy derived from various electrochemical energy devices, including lithium-ion batteries (LIBs), solar cells, fuel cells, and electrochemical capacitors. Despite the various advantages, such as ultrahigh energy density in LIBs, cleanness and permanency in solar cells, high conversion efficiency in fuel cells, some drawbacks also limit their universal applications, including the low power density, high cost, safe issues, and *etc.*[6–8] Hence, the development of novel electrical device is necessary and of high demand. In the recent years, the supercapacitors, also called ultracapacitors or electrochemical capacitors are excellent alternatives, for their special feature in high power density, exceptional cycling stability, rapid charging/discharging rate, and low maintenance costs. However, one bottleneck of supercapacitor is the relatively low energy density compared with LIBs,[9–14] restraining its potential applications to some extents. Thus, how to improve the energy density and at the meantime maintain the high power density and reversibility is the key step to real practical application. As it is known that some works associated with metal-oxide, carbon materials and other composited materials have been proposed to enhance the performance of the supercapacitors from the following aspects: high electrical conductivity, porous structure with high specific surface as well as a hierarchical and well-balanced pore size distribution, superior compatibility with the electrolyte, and high packing density.[15–17]

Graphene has shown broad applied perspective in transparent electronics, space flight, aviation and new energy batteries for its excellent physical chemistry properties namely incredible electronic conductivity, superior mechanical properties and outstanding chemical stability. Last but not least, ultrahigh theoretical specific surface area, which can be up to 2630 $m^2$ $g^{-1}$, renders it one of the most ideal and broad developing prospective candidates as the electrode materials of supercapacitor.[13,18–20]

However, during the processes of materials synthesis and their assembling to capacitors, the high tendency of reaggregation and packing will remarkably decrease the effective specific surface area and astrict the access of electrolyte ions to

*School of Petroleum and Chemical Engineering, Dalian University of Technology, Panjin 124221, Liaoning Province, PR China. E-mail: tanzq@dlut.edu.cn; Tel: +86-427-2631808*

† Electronic supplementary information (ESI) available. See DOI: 10.1039/c6ra27420j

the surface of electrode materials, thus resulting in the performance of graphite instead of graphene.[21,22] Additionally, the pure graphene itself has no band gap, which will be a stumbling block to restrict its developments for various device applications that need bandgap.[18,23] In order to address the above issues and further enhance the performance of the electrochemical capacitors, scientific researchers have focused their attention on developing various methods to enlarge the space between the graphene sheets and open the bandgap of the final materials, such as introducing the intercalation reagents, creating the porous structure, constructing the three dimensional (3D) matrix of graphene-based materials, and heteroatom doping.[7,10,11,24] The feasibility of above mentioned strategies have been proven by vast amounts of representative works, such as graphene/$MnO_2$, graphene/$Co_3O_4$, graphene/polypyrrole, boron and nitrogen doped graphene and so on.[21,25–28] However, to the best of our knowledge, few researches have been presented about the polymer or metal-free carbon materials with relatively high specific capacitance, which will limit their further application in flexible and ultralight electronic field.

In this work, we demonstrated an extremely simple strategy *via* a hydrothermal process to construct the 3D N-doped graphene matrix with the carbon nanotubes (CNTs) and activated carbon (AC) inserting between the layers. For the positive role triggered by each of the component and the synergetic effect between different components in foregoing architecture, the final material exhibits superior performances to the material that lacks any of the components, including the ultrahigh specific area, excellent specific capacitance combined with ultrafast electron transfer and electrolyte transport due to its unique structure with many defects and mesopores on the graphene sheets. These properties may render it as a promising energy storage material in future.

# Experimental

### Synthesis of N-doped graphene/CNTs/AC

The strategy for the synthesis of N-doped graphene/CNTs/AC (NGCA) is presented in Scheme 1. The graphene oxide has been synthesized by a modified Hummers method (for details see ESI†).[29] And the hybrids were fabricated through hydrothermal method. First, the as-synthesized GO samples were dispersed in deionized water (2 mg $mL^{-1}$), which were centrifuged at 8000 rpm to remove the multilayer GO sheets for further use. A dispersion was prepared by consecutive addition of sodium dodecyl benzene sulfonate (SDBS, 0.050 g), single-walled carbon nanotubes (0.016 g) and AC (0.030 g) to $H_2O$ (30.0 mL). Then the dispersion was mixed with the GO suspension (30.0 mL, 2 mg $mL^{-1}$) and followed by ball-milling procedure for 3 h. After above steps, the mixture was prepared by the sonication for 2 h under ice-water bath with $ZrO_2$ balls filling in the flask, to avoid of the temperature rising rapidly. The dispersion was stirred continuously for further 20 minutes. After that, the resulting homogeneous suspension (Fig. 1a) was sealed in a 100.0 mL Teflon-lined stainless-steel autoclave and maintained at 180 °C for 12 h. After it was cooled to room temperature, the black gel was obtained (Fig. 1b), and was immersed in the deionized water (the water was changed every 2 h) for 24 h, ensuring that all the impurities were washed out. Then it was treated by freeze-drying for at least 48 h until the product was sufficiently dried. The obtained aerogel (Fig. 1c) was pyrolyzed at 450 °C under Ar atmosphere for 2 h in a tube furnace to afford the final product.

### Synthesis of N-doped graphene/CNTs, N-doped graphene/AC, graphene/CNTs/AC and RGO

For comparison, N-doped graphene/CNTs (NG/CNTs), N-doped graphene/AC (NG/AC), graphene/CNTs/AC, were prepared following the procedure similar to that of NGCA except that the AC, CNTs, melamine was not added, respectively. And RGO was prepared by the pure GO without adding any other reagent under the same conditions as the NGCA.

### General characterization

Scanning Electron Microscopy (SEM) images were obtained on a FEI Nova NanoSEM 450 field emission scanning electron microscope using an accelerating voltage of 18.00 kV, and Energy Dispersive X-ray Spectroscopy (EDS) was obtained by the AMETEK EDAX detect module on the microscope. Transmission electron microscopy (TEM) was carried out on a FEI Tecnai-$G^2$F30 transmission electron microscope operated at 300 kV. X-ray diffraction (XRD) analyses were carried out on

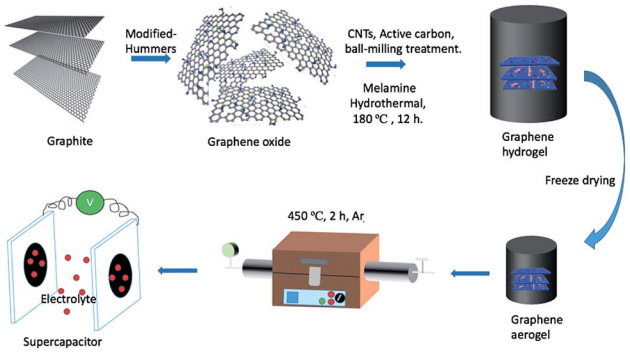


Scheme 1 The strategy for the synthesis of NGCA.

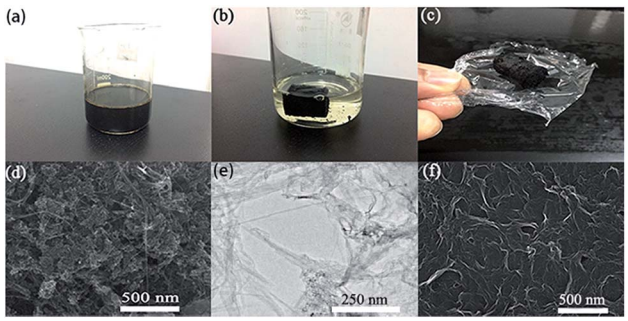


Fig. 1 (a) The mixture before hydrothermal reaction, (b) the hydrogel after the hydrothermal reaction, (c) the aerogel after freeze-drying, (d) SEM of the NGCA, (e) TEM of the NGCA, (f) SEM of the RGO.

a SHIMADZU XRD-7000S diffractometer equipped with Cu $K\alpha_1$ ($\lambda = 1.5406$ Å), in the $2\theta$ range of 0°–90° with the speed of 2° $min^{-1}$. Raman spectra were recorded with a Renishaw inVia Raman spectrometer at 532 nm with an $Ar^+$ laser. The specific surface area and pore size distribution were characterized by nitrogen adsorption–desorption isotherms in a Quantachrome Instruments Autosorb-iQ-C equipment and calculated from desorption data using the Brunauer–Emmett–Teller (BET) method and Barrett–Joyner–Halenda (BJH) model, respectively. X-ray Photoelectron Spectroscopy (XPS) was carried out using a ThermoFisher ESCALAB™250Xi equipment to analyze the chemical composition of the materials. Elemental analysis (EA) was carried out at Vario EL cube (Elementar Analysensysteme GmbH) for determination of the C, H, and O content.

### Electrochemical characterization

All the electrochemical measurements were operated in a conventional three-electrode configuration in 1 M KOH. Cyclic voltammetry (CV) and galvanostatic charge/discharge (GCD) of as-prepared samples were conducted with a CHI660E electrochemical workstation (Chenhua, Shanghai). Electrochemical impedance spectroscopy (EIS) were performed on a SI-1287A/SI-1260A workstation (Solartron Analytical, UK). In a three-electrode system, nickel foam coated with the as-prepared material served as the working electrode, a silver/silver chloride electrode (Ag/AgCl) as the reference, and a platinum sheet electrode as the counter electrode. The working electrode was prepared by mixing the active materials (NGCA or other controllable samples) with polytetrafluoroethylene dispersion (5 wt%) and carbon black at a mass ratio of 8 : 1 : 1 in ethanol. Before painting, the commercial Ni foam ($R = 0.8$ cm) was prewashed with 3 M HCl for 30 min, followed by deionized water several times in an ultrasonic pool. Then the slurry was painted on the Ni foam uniformly and compressed before measurement. The mass loading of the active material in the Ni foam is about 0.6 mg $cm^{-2}$.

## Results and discussion

### Structure and morphology characterization of the hybrids

As shown in Fig. S1,† the RGO hydrogel sank into the bottom of the water, whereas our aimed NGCA hydrogel floated in water (Fig. 1b), indicating that the weight of our NGCA is pretty light (density: 0.042 g $cm^{-3}$). Additionally, the NGCA aerogel can easily be supported by a thin plastic wrap showed in Fig. 1c, further verifying the ultralight physical property. A SEM image in Fig. 1d shows the morphology of NGCA exhibiting a few layers of RGO overlapping each other with the uniform intercalation of CNTs and AC. The structure of NGCA is loose and porous compared with the highly restacked morphology of RGO (Fig. 1f). As shown in Fig. 1e, TEM image of the NGCA with high transparence displays gauze-like and wrinkled morphology, indicating the disordered stack of RGO during the hydrothermal procedure.[30] These results clearly demonstrate the successful intercalation of CNTs and AC into the graphene layers thus leading to the expected sandwich architecture. The unique architecture partly attributed to the enrichment of mesopores in the hybrid, leading to the enhancement of the rate of ion mobility. The nitrogen adsorption–desorption isotherms of the NGCA exhibited typical IV isotherm characteristics with hysteresis loop in the $P/P_0$ range of 0.1–1.0 (Fig. 2a), suggesting that a lot of mesopores do exist in the samples with a very narrow pore size distribution (~4.51 nm, Fig. 2b). Additionally, BET surfaces calculated from the sorption behaviors of the RGO and the NGCA are 610.83 $m^2$ $g^{-1}$ and 952.92 $m^2$ $g^{-1}$, a total pore volume of 0.677 $cm^3$ $g^{-1}$ and 1.075 $cm^3$ $g^{-1}$, respectively.[1,13,15]

The mesoporous structure and the interplanar spacing of the obtained materials were further confirmed by XRD analyses (Fig. 2c). All the samples exhibit the typical peaks of the family of graphite with no other impurities, indicating that our NGCA consists of the pure carbon-based materials. GO shows a sharp diffraction peak at $2\theta = 11.7°$, and the absence of the (002) peak of graphite (about 26°) indicates that the graphite has been fully expanded. The *d*-spacing of 0.75 nm calculated by the Bragg formula, suggests the presence of oxygen-functional groups for the basal plane of the graphene layers in graphite. After hydrothermal carbonization for 12 h, the sharp diffraction peak of GO disappeared. The *d*-spacing value significantly decreased to 0.35 nm, a powerful clue suggesting that most oxygen-functional groups intercalated into the interlayer spacing of graphite were removed.[31] Different from the sharp peak of the RGO, a broad and weak one (002) of the hybrid appears at 25.72°, attributed to the presence of holes in the NGCA sheet and pores in its randomly stacked solid,[32] confirming that nitrogen atoms have been successfully introduced into graphite crystal lattice.[10,33]

In order to characterize the nitrogen doping and disordered degree of carbon in composites, the Raman spectra (Fig. 2d) of RGO and NGCA display two typical main peaks, namely, D- and G-band. The D-band (1350 $cm^{-1}$) is associated with the in-plane bond stretching motion of the pairs of C $sp^2$ atoms (the $E_{2g}$

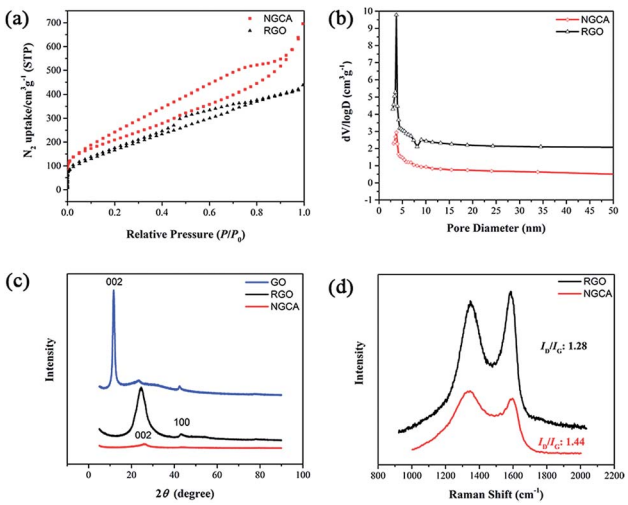


Fig. 2 (a) $N_2$ adsorption/desorption isotherms for NGCA and RGO. (b) Pore size distribution plots (BJH method) for NGCA and RGO. (c) XRD patterns of GO, RGO and NGCA. (d) Raman spectra of RGO and NGCA.

phonons) and shows defects of the $sp^2$ domain in the graphite crystal lattice, while the G-band (1582 $cm^{-1}$) is attributed to the stretching of the C–C bond.[34,35] Similar Raman spectral profiles of RGO and NGCA confirm that the integrity of the graphene layers was not strongly altered during functionalization and the subsequent processing, thus verifying that the NGCA maintain its graphitic domains. The $I_D/I_G$ of NGCA (1.44) higher than that of the RGO (1.28), indicates that the NGCA has more defects, which would lead to a bigger specific surface area and better electrochemical performances.[34,36] According to the literature, the D band frequency will be higher when graphene is doped by nitrogen atoms, and the G band will shift to higher frequency when graphene is stacked fewer layers.[15,37] Compared with the Raman spectrum of RGO, D- and G-bands locations of NGCA are higher by 4.93 $cm^{-1}$ and 6.5 $cm^{-1}$, respectively. The Raman results confirmed that nitrogen atoms have been successfully introduced into graphite crystal lattice that would improve the homogeneous distribution of graphene and CNTs, which is consistent with XRD and SEM analyses.

The EDS mapping of the surface of the NGCA demonstrates the existence and homogeneous distribution of C, O and N elements (Fig. S2†). The oxygen element originates from the oxygen-containing functional groups of graphene oxide, which were not completely reduced during the hydrothermal process. And the existence of nitrogen element demonstrates the nitrogen was doped into the hybrid. The successful introduction of the nitrogen can further be verified by the XPS results. The total survey XPS spectra containing C 1s, O 1s and N 1s further reveal that the hybrid material is composed of these three elements (Fig. 3a). As shown in Fig. 3b, the presence of the C 1s signal was deconvoluted into three peaks centered at 284.39, 284.48, 285.60 eV, corresponding to C=C/C–C, C–OH, C–N bonds, respectively.[38,39] The peak at 285.60 eV originated from N-doping into the defective sites of the NGCA and the small integrated area of C–OH bonds indicates that most of the oxygen-containing groups in the GO raw material have been removed by thermal treatment, resulting in the enhancement of the material's conductivity.[30] As to the high resolution N 1s spectra of the NGCA (Fig. 3c), it can be fitted with three different component peaks at 398.47 eV, 399.73 eV and 401.89 eV, corresponding to pyridinic N, pyrrolic N, and graphitic N, respectively,[40] with their atomic ratio of 35.65 : 35.32 : 29.03. Obviously, nitrogen atoms have not only been doped into the defective sites at the edges but also been incorporated into the in-plane $sp^2$-hybridized carbon framework of graphene sheets.[41,42] As was well documented,[38,43] pyridinic nitrogen and pyrrolic nitrogen, located at the edge of the carbon materials, will induce more disorders of the final carbon materials, which is confirmed by a broad D band in the Raman spectrum. The more distorted graphene materials subsequently display the improved conductivity and electrochemical activity and stability, which are the key factors of electrochemical applications. The technology of elemental analysis was adopted to further evaluate the doping amount of N element precisely, with the total weight ratio of about 7.38% (Table S1†), which is a relatively ideal content in the N-doped materials because that the N content of graphene cannot be infinitely increased. On one hand, high content of doping N leads to the formation of carbon nitride films which have extremely low electrical conductivity; on the other hand, the increasing defects caused by nitrogen doping inevitably lead to the decline of the intrinsic features of graphene.[18] It is notable that the peaks of carbon nitride don't appear in the XRD pattern, demonstrating the appropriate nitrogen content of the NGCA. Fig. 3d shows the deconvoluted XPS spectra of the O 1s from NGCA, having three peaks at 533.40 eV (C–OH), 533.10 eV (O=C) and 531.90 eV (O=C–OH).[38,44,45] And the existence of those oxygen types (Fig. S3†) on the graphene surface play a really significant role in increasing the electrochemical performance of NGCA.[46] These results demonstrate that nitrogen atoms have been successfully doped by the thermal annealing to fabricate the favored nitrogen doped structure, which can improve the wettability of the electrode (graphitic-N) as well as contribute to pseudocapacitance (pyridinic-N/pyrrolic-N).

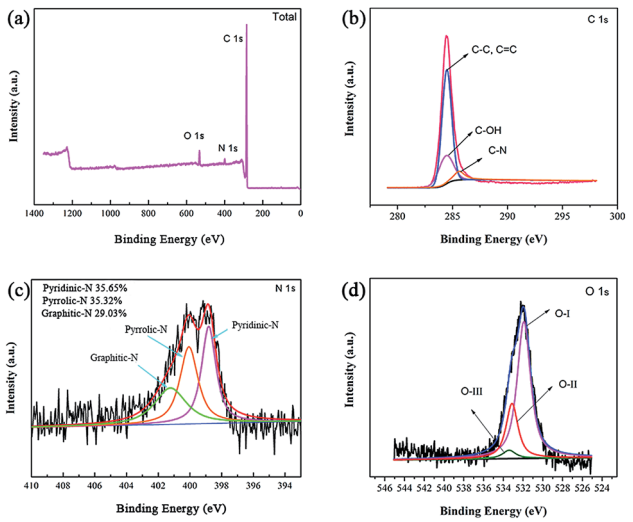


Fig. 3 XPS spectra of NGCA, total spectra (a), spectra of C 1s (b), spectra of N 1s (c) and spectra of O 1s (d).

## Electrochemical performances

To further evaluate the potential application of the NGCA as electrode materials for electrochemical supercapacitors, the NGCA and other controllable samples were examined first in a three-electrode system, where a 1 M aqueous KOH solution was used as electrolyte. As shown in Fig. 4a, CV measurements of NGCA were carried out between −0.8 and 0.3 V (*vs.* Ag/AgCl) at various scan rates ranging from 10 to 200 mV $s^{-1}$. The shapes of the CV curves still remains close to rectangle even at the scan rate of 200 mV $s^{-1}$, indicating that the NGCA has an excellent rate capability and the capacitance characteristics are similar to that of the electric double-layer capacitance.[41,47,48] Faradaic peaks, corresponding to the redox reactions of the nitrogen doping and residual oxygen-containing groups, were observed in the CV curves, obviously implying the coexistence of electric double layer capacitance and pseudocapacitance.[46,49] And the CV curves with lower scan rates present the well-defined distinct

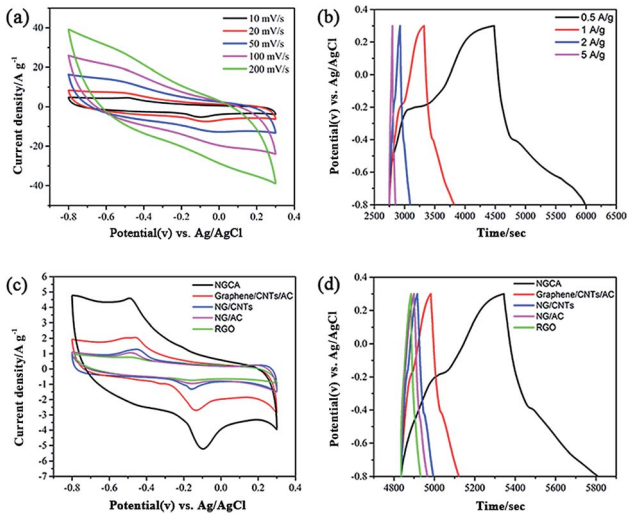


Fig. 4 Electrochemical characterizations of samples in a three-electrode configuration (1 M KOH): (a) CV curves of NGCA at different scan rates, (b) GCD curves of NGCA at different current densities, (c) CV curves of the five samples at a scan rate of 10 mV $s^{-1}$, (d) GCD curves of all samples at 1 A $g^{-1}$.

redox peaks because the diffusion rates of electrolyte ions are limited by electrode structural properties. At lower scan rates, all the active areas, including external and internal surfaces, can be utilized for charge/discharge and electrochemical utilization. However, only the external sites can take part in ion transfer reaction when operating at high scan rates.[41] The GCD curve of NGCA shows a deviation from the ideal triangle shape (Fig. 4b), further confirming the inspiring contribution of pseudocapacitance accorded with the CV results. The comparison of CV and GCD curves between the NGCA and hybrids with different components are presented in Fig. 4c and d, respectively. The maximum CV area response and GCD discharge time span of NGCA reflect its optimal capacitance property due to the synergistic effect among the CNTs, AC and NG. Comparation on other hybrids with different components (Table S2†), the NGCA has the largest specific capacitance 466 F $g^{-1}$ at a current density of 1 A $g^{-1}$ calculated by the discharge curve. When operating at a smaller current density (0.5 A $g^{-1}$), the specific capacitance can reach to 750 F $g^{-1}$ which is matched with the reported relevant superior works,[30,38,43,48] and higher than some of them (Table 1).[36,50–52] To explore the effect of nickel disk itself to the capacitance, the blank experiment (reference) is undertaken, using the nickel sheet (without active material) as working electrode in the same condition. The CV curves are shown in Fig. S4.† There are no obvious redox peaks in the CV curve of pure Ni foam, which indicates that the NiOOH/$Ni(OH)_2$ redox has no contribution to our capacitance in the experimental condition. Furthermore, the typical value of capacitance of nickel sheet is calculated to be 1.59 F $g^{-1}$. So the contribution of nickel sheet can be ignored in our experiments. Above results indicate the positive role played by each component. First, N doping has opened the band gap, thus enhancing the redox reactions between the electrolyte ions and hydroquinone molecules;[11,38,53,54] According to the calculation of the binding energy between the potassium ion and nitrogen configurations, the basal-plane pyridinic N and pyrrolic N have larger binding energy with potassium ion, leading to a larger number of ions to be accommodated on the electrode surface. Therefore, the supercapacitor performance was enhanced.[49] Secondly, because of the existence of the strong van der Waals forces and π–π interactions between the adjacent graphene sheets, they tend to restack together during the processes of materials preparation under hydrothermal condition and electrode making. However, the inserted CNTs would serve as a supporting bridge to restrain the agglomeration, also provide the path of ion transport to shorten the distance of ion diffusing into the electrode by the hollow tubular structure. Thirdly, AC would increase the packing density of the overall hybrids and also act as fixed bolt balls to prevent the carbon nanotube creeping down from the graphene layers, thus improving the cycling stability of the electrode materials.[12]

EIS is one of the principal methods to examine the charge transfer and ion transport between the electrode materials and electrolyte. As shown in Fig. 5a, in the frequency range from 100 kHz to 10 MHz, a semicircle at high frequency following a diagonal at low frequency is observed for each sample. The semicircles in the high-frequency region reflect the existence of the charge transfer resistance ($R_{ct}$), the smaller diameter of semicircle, the easier charge transfer between electrode and electrolyte.[55] As shown in Table S2,† the $R_{ct}$ (0.26) of the NGCA is much lower than the controllable samples, corresponding to a smaller semicircle, indicating that it can offer faster charge transportation, which can be contributed to the desired N structures as discussed above. Furthermore, a lower diffusion resistance of electrolyte ions makes the diagonal lines closer to 90° in Nyquist plots at low frequency, and the electrode materials behave more closely to an ideal capacitor.[27,46] The nearly vertical lines of NGCA reflects that the double-layer structure can be established rapidly, indicating a fast ion transfer

Table 1 Specific capacitance for some graphene-based materials reported in literature

| Relevant works | Electrolyte | $C_m$ (F $g^{-1}$) | Ref. |
|---|---|---|---|
| Holey graphene/polypyrrole nanoparticle hybrid aerogels | KOH (1 M) | 418 (0.5 A $g^{-1}$) | 21 |
| N-Doped active carbon fiber@graphene composites | KOH (6 M) | ≈475 (0.5 A $g^{-1}$) | 36 |
| Nitrogen-doped graphene/carbon nanotubes composite | KOH (6 M) | 246.6 (0.5 A $g^{-1}$) | 15 |
| GN/MCS composite film | KOH (1 M) | ≈203 (0.5 A $g^{-1}$) | 26 |
| Layered molybdenum sulfide/N-doped graphene hybrid | KOH (1 M) | ≈232 (0.5 A $g^{-1}$) | 46 |
| NGCA | KOH (1 M) | 750 (0.5 A $g^{-1}$) | This work |

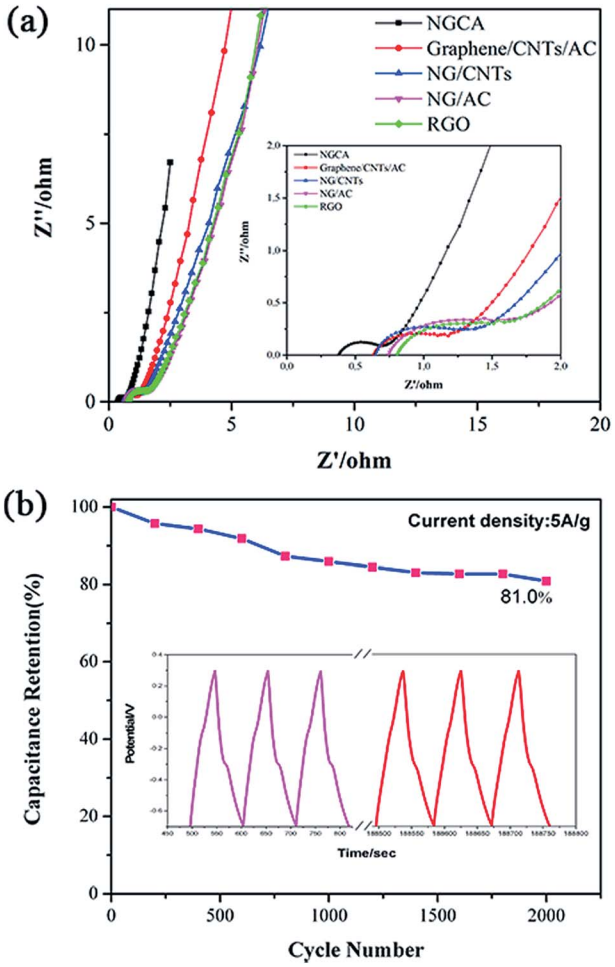


Fig. 5 (a) Nyquist plots of the NGCA and RGO. (b) Cyclic performance of NGCA at 5 A $g^{-1}$, the inset shows the GCD curves of the first three cycles and last three cycles.

kinetics. The equivalent circuit for the fitting of the EIS data is presented in Fig S6,† $R_s$ is the resistance derived from the electrolyte and the contact between the electrode and the current collector. $C_{dl}$ is a double-layer capacitor. The excellent dynamic behavior is believed to be closely linked to the good wettability of materials benefiting from the suitable oxygen contents (~12 at%) calculated by the XPS spectra and the hydrophilic groups (*i.e.*, carboxyl groups) incorporated in the carbon networks.[18] The cyclic stability of supercapacitor is no exception a vital criterion for its practical applications. Thus, the long-term cyclic stability of the NGCA was evaluated by repeating the galvanostatic charge/discharge test between −0.8 V to 0.3 V at a current density of 5 A $g^{-1}$ for 2000 cycles. Fig. 5b shows that our NGCA-based supercapacitor exhibits rather promising cycle stability, approximate 81% capacitance retention at such a high current density, attributed to the unique structure created by the nitrogen-doping and CNT/AC-supporting. From the inset curve of Fig. 5b, to observe carefully, the redox character of GCD curves in last three cycles become invisible compared with those in the initial cycles, demonstrating that the main decrease in capacitance is due to the gradual loss of the pseudocapacitance as the cycles increase. Hence, the easy-synthesized NGCA possesses good comprehensive electrochemical properties as an electrochemical capacitor electrode material to harvest energy.

## Conclusions

In summary, a three dimensional N-doped graphene/CNTs/AC composite has been fabricated by the combination of one-step hydrothermal method and a series of assistant optimization process using GO as the precursors and CNTs, AC and melamine as the mediator. In the resultant hybrid, disordered NG nanosheets were uniformly decorated with CNTs and AC, forming a sandwich structure with hierarchal mesopores, large surface area and high conductive network. It presents the excellent electrochemical performances as a supercapacitor electrode material such as ultrahigh specific capacitance, good cycle stability. Therefore, the as-prepared N-doped graphene/CNTs/AC composite is a promising electrode material for supercapacitor to harvest energy in the future.

## Acknowledgements

This work was supported by the National Natural Science Foundation of China (NSFC Nos. 21571028) and the Fundamental Research Funds for the Central Universities (No. DUT15RC(3)055 and No. DUT15RC(3)040).

## References

1 K. Yuan, Y. Xu, J. Uihlein, G. Brunklaus, L. Shi, R. Heiderhoff, M. Que, M. Forster, T. Chasse, T. Pichler, T. Riedl, Y. Chen and U. Scherf, *Adv. Mater.*, 2015, **27**, 6714–6721.
2 R. Kumar, H.-J. Kim, S. Park, A. Srivastava and I.-K. Oh, *Carbon*, 2014, **79**, 192–202.
3 T. Zhang, F. Zhang, L. Zhang, Y. Lu, Y. Zhang, X. Yang, Y. Ma and Y. Huang, *Carbon*, 2015, **92**, 106–118.
4 L. Zhang, K. N. Hui, K. San Hui and H. Lee, *J. Power Sources*, 2016, **318**, 76–85.
5 J. H. Lee, N. Park, B. G. Kim, D. S. Jung, K. Im, J. Hur and J. W. Choi, *ACS Nano*, 2013, **7**, 9366–9374.
6 F. Bonaccorso, L. Colombo, G. Yu, M. Stoller, V. Tozzini, A. C. Ferrari, R. S. Ruoff and V. Pellegrini, *Science*, 2015, **347**, 1246501.
7 C. Liu, Z. Yu, D. Neff, A. Zhamu and B. Z. Jang, *Nano Lett.*, 2010, **10**, 4863–4868.
8 M. Zhang, R. Li, X. Chang, C. Xue and X. Gou, *J. Power Sources*, 2015, **290**, 25–34.
9 W. Yang, M. Ni, X. Ren, Y. Tian, N. Li, Y. Su and X. Zhang, *Curr. Opin. Colloid Interface Sci.*, 2015, **20**, 416–428.
10 Y.-Y. Peng, Y.-M. Liu, J.-K. Chang, C.-H. Wu, M.-D. Ger, N.-W. Pu and C.-L. Chang, *Carbon*, 2015, **81**, 347–356.
11 H. Huang, C. Lei, G. Luo, Z. Cheng, G. Li, S. Tang and Y. Du, *J. Mater. Sci.*, 2016, **51**, 6348–6356.
12 C. Zheng, X. Zhou, H. Cao, G. Wang and Z. Liu, *J. Power Sources*, 2014, **258**, 290–296.

13 V. Sahu, S. Shekhar, R. K. Sharma and G. Singh, *ACS Appl. Mater. Interfaces*, 2015, **7**, 3110–3116.
14 J. Li, X. Zhang, R. Peng, Y. Huang, L. Guo and Y. Qi, *RSC Adv.*, 2016, **6**, 54866–54873.
15 T.-T. Lin, W.-H. Lai, Q.-F. Lü and Y. Yu, *Electrochim. Acta*, 2015, **178**, 517–524.
16 A. Lamberti, A. Gigot, S. Bianco, M. Fontana, M. Castellino, E. Tresso and C. F. Pirri, *Carbon*, 2016, **105**, 649–654.
17 P. R. Agarwal, R. Kumar, S. Kumari and S. R. Dhakate, *RSC Adv.*, 2016, **6**, 100713–100722.
18 B. Xie, Y. Chen, M. Yu, X. Shen, H. Lei, T. Xie, Y. Zhang and Y. Wu, *Nanoscale Res. Lett.*, 2015, **10**, 1031.
19 H. Chen, H. Gao, H. Xiao, X. Zhou, W. Zhang and Q. Ling, *Electrochim. Acta*, 2016, **206**, 10–16.
20 J. Zhang, H. Zhang, Y. Cai and H. Zhang, *RSC Adv.*, 2016, **6**, 98010–98017.
21 Y. He, Y. Bai, X. Yang, J. Zhang, L. Kang, H. Xu, F. Shi, Z. Lei and Z.-H. Liu, *J. Power Sources*, 2016, **317**, 10–18.
22 S. Wang, L. Zhang, C. Sun, Y. Shao, Y. Wu, J. Lv and X. Hao, *Adv. Mater.*, 2016, **28**, 3768–3776.
23 D. Akinwande, N. Petrone and J. Hone, *Nat. Commun.*, 2014, **5**, 5678.
24 Y. Xu, K. Sheng, C. Li and G. Shi, *ACS Nano*, 2010, **4**, 4324–4330.
25 Y. Ding, J. Zhu, C. Wang, B. Dai, Y. Li, Y. Qin, F. Xu, Q. Peng, Z. Yang, J. Bai, W. Cao, Y. Yuan and Y. Li, *Carbon*, 2016, **104**, 133–140.
26 X. Lu, H. Dou and X. Zhang, *Mater. Lett.*, 2016, **178**, 304–307.
27 A. Ouyang, A. Cao, S. Hu, Y. Li, R. Xu, J. Wei, H. Zhu and D. Wu, *ACS Appl. Mater. Interfaces*, 2016, **8**, 11179–11187.
28 S. Yang, Y. Lin, X. Song, P. Zhang and L. Gao, *ACS Appl. Mater. Interfaces*, 2015, **7**, 17884–17892.
29 G. Jiang, M. Goledzinowski, F. J. E. Comeau, H. Zarrin, G. Lui, J. Lenos, A. Veileux, G. Liu, J. Zhang, S. Hemmati, J. Qiao and Z. Chen, *Adv. Funct. Mater.*, 2016, **26**, 1729–1736.
30 Z. Wen, X. Wang, S. Mao, Z. Bo, H. Kim, S. Cui, G. Lu, X. Feng and J. Chen, *Adv. Mater.*, 2012, **24**, 5610–5616.
31 X. Ye, Q. Zhou, C. Jia, Z. Tang, Z. Wan and X. Wu, *Electrochim. Acta*, 2016, **206**, 155–164.
32 Z.-J. Jiang, Z. Jiang and W. Chen, *J. Power Sources*, 2014, **251**, 55–65.
33 X. Wu, D. Yang, C. Wang, Y. Jiang, T. Wei and Z. Fan, *Carbon*, 2015, **92**, 26–30.
34 P. Iamprasertkun, A. Krittayavathananon and M. Sawangphruk, *Carbon*, 2016, **102**, 455–461.
35 J. Li, G. Zan and Q. Wu, *RSC Adv.*, 2016, **6**, 57464–57472.
36 P. Ramakrishnan and S. Shanmugam, *J. Power Sources*, 2016, **316**, 60–71.
37 P. Bharathidasan, D.-W. Kim, S. Devaraj and S. R. Sivakkumar, *Electrochim. Acta*, 2016, **204**, 146–153.
38 Q. Xie, R. Bao, C. Xie, A. Zheng, S. Wu, Y. Zhang, R. Zhang and P. Zhao, *J. Power Sources*, 2016, **317**, 133–142.
39 Y. Bai, R. B. Rakhi, W. Chen and H. N. Alshareef, *J. Power Sources*, 2013, **233**, 313–319.
40 Z. Y. Sui, Y. N. Meng, P. W. Xiao, Z. Q. Zhao, Z. X. Wei and B. H. Han, *ACS Appl. Mater. Interfaces*, 2015, **7**, 1431–1438.
41 S. S. Balaji, A. Elavarasan and M. Sathish, *Electrochim. Acta*, 2016, **200**, 37–45.
42 Y. Song, J. Yang, K. Wang, S. Haller, Y. Wang, C. Wang and Y. Xia, *Carbon*, 2016, **96**, 955–964.
43 S.-M. Li, S.-Y. Yang, Y.-S. Wang, H.-P. Tsai, H.-W. Tien, S.-T. Hsiao, W.-H. Liao, C.-L. Chang, C.-C. M. Ma and C.-C. Hu, *J. Power Sources*, 2015, **278**, 218–229.
44 N. Xiao, D. Lau, W. Shi, J. Zhu, X. Dong, H. H. Hng and Q. Yan, *Carbon*, 2013, **57**, 184–190.
45 L. Lai, H. Yang, L. Wang, B. K. Teh, J. Zhong, H. Chou, L. Chen, W. Chen, Z. Shen and R. S. Ruoff, *ACS Nano*, 2012, **6**, 5941–5951.
46 B. Xie, Y. Chen, M. Yu, T. Sun, L. Lu, T. Xie, Y. Zhang and Y. Wu, *Carbon*, 2016, **99**, 35–42.
47 W. Zhang, Z. Yin, A. Chun, J. Yoo, G. Diao, Y. S. Kim and Y. Piao, *J. Power Sources*, 2016, **318**, 66–75.
48 B. You, F. Kang, P. Yin and Q. Zhang, *Carbon*, 2016, **103**, 9–15.
49 P. Chen, J.-J. Yang, S.-S. Li, Z. Wang, T.-Y. Xiao, Y.-H. Qian and S.-H. Yu, *Nano Energy*, 2013, **2**, 249–256.
50 J. Zhu, Y. Xu, Y. Zhang, T. Feng, J. Wang, S. Mao and L. Xiong, *Carbon*, 2016, **107**, 638–645.
51 X. Wang, C. Lu, H. Peng, X. Zhang, Z. Wang and G. Wang, *J. Power Sources*, 2016, **324**, 188–198.
52 M. G. Hosseini and E. Shahryari, *J. Mater. Sci. Technol.*, 2016, **32**, 763–773.
53 C. Chen, W. Fan, T. Ma and X. Fu, *Ionics*, 2014, **20**, 1489–1494.
54 Y.-P. Lin, Y. Ksari, J. Prakash, L. Giovanelli, J.-C. Valmalette and J.-M. Themlin, *Carbon*, 2014, **73**, 216–224.
55 J. Zhang, Z. Yang, X. Wang, T. Ren and Q. Qiao, *RSC Adv.*, 2016, **6**, 84847–84853.